Speciation and Structures in Pt Surface Sites Stabilized by N-Heterocyclic Carbene Ligands Revealed by Dynamic Nuclear Polarization Enhanced Indirectly Detected 195 Pt NMR Spectroscopic Signatures and Fingerprint Analysis

Zhuoran Wang, Laura Völker, Thomas Robinson, Nicolas Kaeffer, Georges Menzildjian, Ribal Jabbour, Amrit Venkatesh, David Gajan, Aaron J Rossini, Christophe Copéret, et al.

Speciation and Structures in Pt Surface Sites Stabilized by N-Heterocyclic Carbene Ligands Revealed by DNP Enhanced Indirectly Detected ^{195}Pt NMR Spectroscopic Signatures and Fingerprint Analysis

Zhuoran Wang,[†#] Laura A. Völker,[§#] Thomas Robinson,[†] Nicolas Kaeffer,[§¥] Georges Menzildjian,[†] Ribal Jabbour,[†] Amrit Venkatesh,[‡o] David Gajan,[†] Aaron J. Rossini,[‡o*] Christophe Copéret,[§*] Anne Lesage[†*]

[†] Université de Lyon, CNRS, ENS Lyon, Université Lyon 1, Centre de RMN à hauts champs de Lyon, UMR 5082, F-69100, 5 rue de la Doua, 69100 Villeurbanne, France

[§] ETH Zürich, Department of Chemistry and Applied Biosciences, Vladimir-Prelog-Weg 1-5/10, 8093 Zürich, Switzerland

[‡] Department of Chemistry, Iowa State University, Ames IA, USA.

[o] U.S. DOE Ames Laboratory, Ames IA, USA.

[¥] Current address: Max Planck Institute for Chemical Energy Conversion, 45470 Mülheim an der Ruhr, Germany.

[#] Authors equally contributed.

* To whom correspondence should be addressed.

ABSTRACT: N-Heterocyclic carbenes (NHCs) are widely used ligands in transition metal catalysis. Notably, they are increasingly encountered in heterogeneous systems. While a detailed knowledge of the possibly multiple metal environments would be essential to understand the activity of metal-NHC-based heterogeneous catalysts, only a few techniques currently have the ability to describe with atomic-resolution structures dispersed on a solid support. Here, we introduce a new DNP surface enhanced solid-state NMR approach that, in combination with advanced DFT calculations, allows the structure characterization of isolated silica-supported Pt-NHC sites. Notably, we demonstrate that the signal amplification provided by DNP in combination with fast magic angle spinning enables the implementation of sensitive ^{13}C-^{195}Pt correlation experiments. By exploiting $^{1}J(^{13}C\text{-}^{195}Pt)$ couplings, 2D NMR spectra were acquired revealing two types of Pt sites. For each of them, $^{1}J(^{13}C\text{-}^{195}Pt)$ values were determined as well as ^{195}Pt chemical shift tensor parameters. To interpret the NMR data, DFT calculations were performed on an extensive library of molecular Pt-NHC complexes. While one surface site was identified as a bis-NHC compound, the second site most likely contains a bidentate 1,5 cyclooctadiene ligand, pointing to various parallel grafting mechanisms. The methodology described here represents a new step forward in the atomic-level description of catalytically relevant surface metal-NHC complexes. In particular, it opens up innovative avenues for exploiting the spectral signature of platinum, one of the most widely used transition metals in catalysis, but whose use for solid-state NMR remains difficult. Our results also highlight the sensitivity of ^{195}Pt NMR parameters to slight structural changes.

INTRODUCTION

N-Heterocyclic carbenes (NHCs) have been developed in the past three decades as an important class of ligands in homogeneous catalysis, as they are strong neutral s-donor ligands, making stable chemical bonds with ranges of metals.[1, 2] They have more recently been used in heterogeneous catalysis either to immobilize organometallic complexes on materials such as polymers or oxides,[3-6] or to tune the catalytic performance of supported metal nanoparticles.[7-13] Highly active and robust heterogeneous catalysts have been prepared based on the concept of supported homogeneous catalysis (SHC), where the metal sites are introduced through the post-functionalization of already immobilized imidazolium compounds yielding metal sites attached to NHC ligands anchored to the support. Such organic ligands or their precursors are preferentially incorporated by a direct synthesis method or by the modification of an oxide support by a sol-gel process because it has been shown that these processes lead to a more homogenous distribution of the organic ligands at the surface of the silica matrix (support).[14-16] This approach has been successfully employed to prepare a range of highly efficient catalysts, for reactions such as olefin metathesis and hydrogenation, or CO_2 reduction.[17-20] While the SHC approach aims at generating single-site catalysts with well-defined coordination environment around the metal centers to mimic their molecular analogues developed for homogeneous processes, there is growing evidence that unexpected or multiple structures can form due to the inherent complexity of surface chemistry. For example, interactions may occur between the metal centers and the surface functionalities of the solid support that modify the coordination environment around the active sites as observed for an immobilized Ru-NHC catalyst.[21] Furthermore, metal sites may be bonded to one or several organic ligands as recently shown

on a supported Ir-NHC complex where two types of surface organometallic sites were identified, with the Ir metal centers bound to one or two NHC surface ligands.[22] Yet, despite the evidences of various surface sites, obtaining a precise understanding of the structure and coordination environment of metal sites in supported catalysts remains a challenge and a critical aim. Thus, developing methodologies that enable identifying both speciation and describing the coordination environment of metal sites is of prime importance to understand and further improve catalytic performance of supported catalysts, paralleling the realm of molecular chemistry and homogeneous catalysis.

Over the last twenty years, solid-state NMR spectroscopy, often in combination with Fourier transform infrared (FTIR) spectroscopy, extended X-ray absorption fine structure (EXAFS) or X-ray absorption near edge structure (XANES) has emerged as a unique analytical method to probe the atomic-scale structure of active sites in heterogeneous catalysts.[23-25] The recent advent of high-field dynamic nuclear polarization (DNP) has further reinforced the analytic power for surfaces.[26-30] This approach indeed yields tremendous gains in signal-to-noise ratio, favoring surface sites, and enables the implementation of advanced NMR methodologies, even on dilute substrates. In the field of supported molecular catalysts, DNP surface enhanced NMR spectroscopy (DNP SENS) [31, 32] has thus been successfully applied to characterize a variety of systems, such as highly reactive metal sites directly anchored on the surface of silica or alumina,[33-39] or atop metallic nanoparticles.[12] Several DNP SENS studies have also been carried out on metal-NHC complexes, providing invaluable structural information, focusing mostly on understanding the conformation of metal sites within the pores of the support.[12, 40-43]

Conventional and DNP enhanced solid-state NMR studies aiming at investigating the structure of metal complexes supported on surfaces, i.e., portraying the coordination sphere of metal sites on surfaces predominately focus on the (organic) ligands. The structure around the metal center is typically probed by one- and two-dimensional experiments involving nuclei such as ^{1}H, ^{13}C, ^{15}N, ^{29}Si or ^{31}P depending on the ligands. Information on isotropic chemical shift (δ_{iso}), chemical shift anisotropy (CSA), dipolar or quadrupolar couplings is usually obtained and compared with data on molecular analogs. When the metal center is NMR active, its spectral signature also provides a rich and complementary source of structural information, and a few ^{27}Al, ^{45}Sc, ^{51}V, ^{89}Y, ^{93}Nb, ^{119}Sn or ^{195}Pt NMR studies have been reported on supported complexes.[24, 35, 37, 44-51] The NMR interactions experienced by the metal center are sensitive to slight changes of the coordination sphere and therefore provide a direct insight into its electronic structure. In particular, some coordination structures may be overlooked when only the NMR signatures of the ligands are taken into account.

Platinum is one of these metal centers at the core of many heterogeneous catalysts that can be probed directly by solid-state NMR spectroscopy. However, until recently, despite the favorable spectroscopic properties of ^{195}Pt (a spin quantum number of I=1/2 and a relatively high receptivity), only a few investigations have considered platinum NMR due to its large CSA (leading to broad spectral signatures) combined with the low concentration of sites, that makes this spectroscopy extremely insensitive. This limitation could be very recently overcome with DNP, and DNP enhanced ^{195}Pt spectra have been reported on a handful of organometallic complexes under static or magic angle spinning (MAS) conditions.[37, 39, 50, 52] As an alternative approach, we have just demonstrated that the ^{195}Pt NMR signature of surface metal centers could be indirectly detected through sensitive spy nuclei such as ^{1}H or ^{31}P.[53] We further showed that ^{195}Pt sideband-selective saturation/excitation pulses could be incorporated into ^{1}H-^{195}Pt double resonance experiments to reconstruct MAS ^{195}Pt solid-state NMR spectra of single-site supported materials.

Here, we capitalize on these recent achievements and develop a methodology to readily assess the speciation and the structure of surface sites in Pt(II)-NHC complex immobilized on a mesoporous silica surface. This has been made possible by acquiring a series of complementary NMR signatures, namely isotropic chemical shifts of various nuclei (^{13}C and ^{195}Pt), chemical shift anisotropy (Ω_{Pt}, κ_{Pt}), J-coupling constant ($J_{Pt\text{-}C}$), and by solving the structure by matching these multiple spectral signatures to expected values from a large computational library by regression analysis. We choose this material as a prototypical example of heterogeneous catalysts, and show the presence of two Pt sites, corresponding to mono- and bis-grafted species, in the cationic and neutral form, respectively. Detailed analysis of the NMR signatures by computational approaches also enables us to provide guiding principles to decipher the general coordination environment of NHC-Pt-based systems that can be encountered in both homogeneous and heterogeneous systems and to refine the structure of the supported systems.

RESULTS AND DISCUSSION

Pt-material. A hybrid silica material with ^{13}C-labeled pendant imidazolium ligands at the C6 position was prepared[40, 54] and passivated by protection of the silanol groups with deuterated trimethylsilyl functionalities (**NHC@SiO₂**). The introduction of Pt was then carried out via deprotometallation using $[Ag(OC(CF_3)_3)]$ followed by transmetallation with $[Pt(COD)Cl_2]$ as a molecular precursor. The resulting immobilized Pt(II)-NHC complex is referred to as **Pt(NHC)@SiO₂**; its synthesis is schematically illustrated in Figure 1a and was performed following reported procedure[40] (details regarding the preparation of the materials are provided in the Supporting Information (SI)). Of note, elemental analysis of **Pt(NHC)@SiO₂** allows the estimation of an atomic ratio of 1:3.4:3.9 Pt/N/Cl in the final material. The Pt/Cl and Pt/N ratios being lower than 1:2 indicate that more than one NHC/imidazolium chloride moiety is present per Pt site.

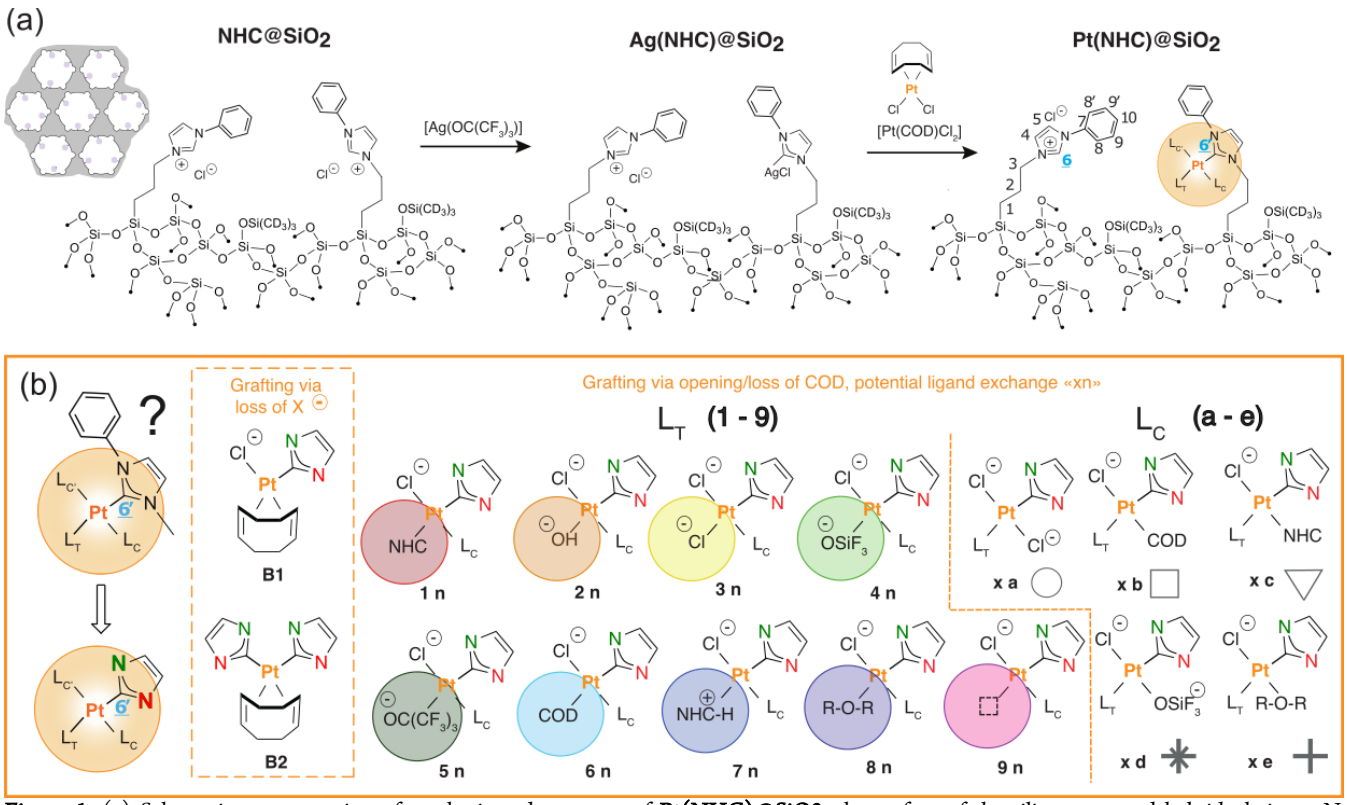

Figure 1. (a) Schematic representation of synthesis and structure of **Pt(NHC)@SiO2**, the surface of the silica-supported hybrid platinum N-heterocyclic carbene material investigated here. The full synthetic pathway is described in the SI. The numbers used to identify the various carbons are indicated. The positions where a ^{13}C label was introduced are labeled in blue and underlined. The structure of the silica support is depicted in the insert on the left-hand side of the scheme. (b) Potential structures that could be formed around the Pt center after adding [Pt(COD)Cl**2**] onto the pre-functionalized silica material were investigated by means of DFT studies on a library of molecular model compounds containing a variety of ligands in trans (L_t) and cis (L_c) positions of the NHC ligand. The conventions used for labelling of the compounds and graphical analysis of the DFT results are indicated. The structures are labelled using a two-letter code of type **xn** where x = 1-9 indicates L_t and n = a-e refers to L_c. In **8n** and **xe,** R-O-R stands for $F_3Si\text{-}O\text{-}Si(CH_3)_3$. In the molecular models the two nitrogen atoms are recpectively bonded to a phenyl and a methyl group as represented in the left-hand side of the figure.

DNP enhanced ^{13}C and ^{195}Pt NMR spectroscopy. For the DNP SENS experiments carried out at 9.4 T, **Pt(NHC)@SiO₂** was impregnated by a 16 mM TEKPol solution in 1,1,2,2-tetracholoroethane (TCE) and packed into a 1.3 mm ZrO_2 rotor. A solvent DNP signal enhancement factor (ε) of 96 was measured at 36 kHz MAS frequency. Figure 2a shows the one-dimensional (1D) ^{13}C spectrum of **Pt(NHC)@SiO₂**. The resonances of the propyl chain (see inset) and of the imidazole and aromatic carbons can be readily identified according to previous studies.[40] In particular, at high chemical shifts, two intense resonances are observed that correspond to the (^{13}C labelled) C6 of the 1-phenyl-3-propylimidazolium (chloride) ionic group precursor (at 138 ppm) and to the coordinating C6' of the Pt-NHC complex (at 178 ppm). The presence of a significant residual fraction of unreacted imidazolium groups could be revealed here thanks to the ^{13}C isotopic enrichment at the carbene position (≥ 66% ^{13}C), in contrast to previous studies where these signals overlap and could not be identified.[40] The C6' resonance at 178 ppm exhibits two satellite peaks that correspond to the fraction of carbon nuclei bonded to the NMR active ^{195}Pt isotope (natural abundance 33.8%).

We have recently shown that the ^{195}Pt NMR signature of surface complexes could be extracted from static ^{195}Pt DNP SENS spectra[39] or, with a great benefit in terms of sensitivity, from proton-detected heteronuclear correlation spectroscopy at fast MAS frequencies.[53] In particular, we demonstrated that a series of sideband selective experiments could be applied to expeditiously probe the ^{195}Pt CSA pattern from the resonances of adjacent, dipolar-coupled protons. However, their implementation requires the presence of protons in close proximity of the Pt center as their efficiency is proportional to the strength of dipolar couplings between ^{1}H and ^{195}Pt spins. Such a condition is not always met, as is the case for the Pt-NHC complexes investigated here. Alternatively, we showed that other sensitive spy nuclei such as ^{31}P could be exploited.[53] In this study, by capitalizing on the sensitivity improvement provided by DNP, we show that ^{195}Pt NMR parameters (the isotopic chemical shifts, the CSA values and the scalar coupling with bonding carbon atom) can be indirectly detected on ^{13}C nuclei. This is achieved by implementing a set of experiments that are described below.

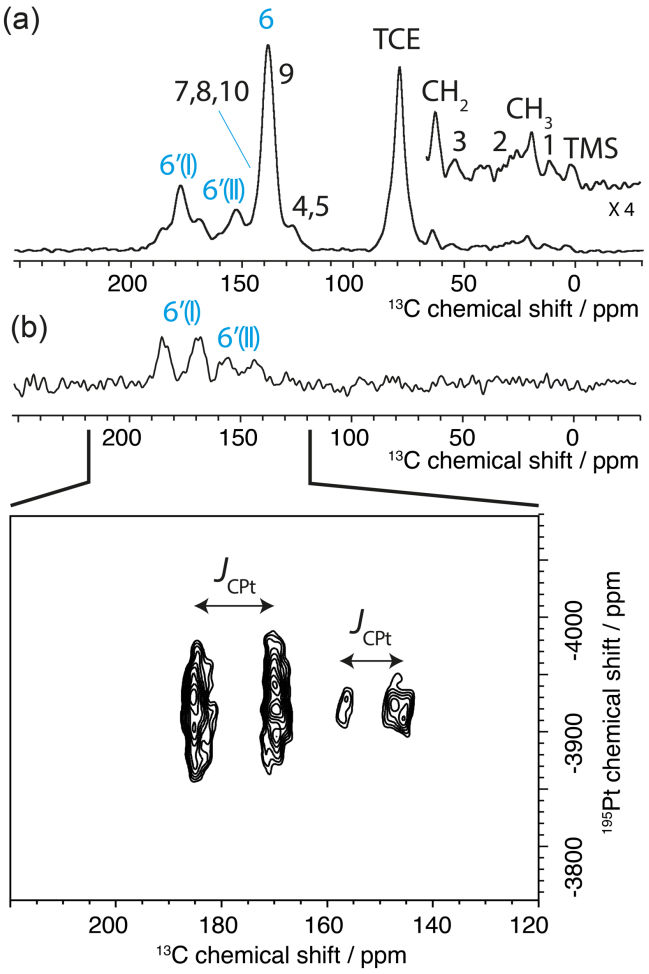

Figure 2. (a) 1D DNP enhanced $^{13}C\{^{1}H\}$ CPMAS spectrum of **Pt(NHC)@SiO₂**. The CH_2 and CH_3 resonances correspond to traces of residual O-ethyl groups. The C6 and C6' resonances observed respectively for the unreacted imidazolium fragement and for the Pt-NHC complex are labelled in blue. The spectrum was acquired at a MAS frequency of 36 kHz. (b) 1D and 2D DNP enhanced $^{13}C\{^{195}Pt\}$ *J*-HMQC spectra. Two distinct Pt sites are revealed. The spectrum was recorded at a MAS frequency of 36 kHz. The 1D and 2D spectra were recorded in respectively 25 minutes and 64 hours. Other experimental details are reported in the SI.

We first implemented a DNP enhanced carbon-detected through-bond heteronuclear multiple quantum correlation[55, 56] experiment (*J*-HMQC). The corresponding pulse sequence is shown in Figure S3 in the SI. Figure 2b (top) shows the 1D $^{13}C\{^{195}Pt\}$ *J*-HMQC spectrum ($t_1 = 0$) of **Pt(NHC)@SiO₂** recorded with *J* coupling evolution and reconversion delays τ_J of 0.25 ms. These delays were optimized for maximizing the coordinated carbene signal intensity. As no ^{195}Pt decoupling was applied during the acquisition of the ^{13}C free induction decay (FID), the ^{13}C resonances bound to ^{195}Pt spins appear as doublets separated by the ^{13}C-^{195}Pt scalar couplings of about ~1600 Hz and ~1200 Hz for ^{13}C signals (I) and (II), respectively (an accurate measurement of these couplings was performed later, see Figure 3 below). The efficiency of $^{13}C\{^{195}Pt\}$ *J*-HMQC experiment was estimated to be around 30%, by comparing the signal intensities in 1D CPMAS and *J*-HMQC spectra, which agrees with numerical simulation result (Figure S4 in the SI). The efficiency of the through-bond transfer in *J*-HMQC experiment depends mainly on the strength of ^{195}Pt radio-frequency (RF) pulse and the transverse coherence lifetimes (T_2') of the directly detected ^{13}C nuclei. The highest tolerable RF field, ca. 200 kHz, was used for ^{195}Pt pulses to maximize the efficiency. A T_2' value of 21 ms was determined here for the carbene C6′ resonances (Figure S5 in the SI), corresponding to a refocused linewidth of 15 Hz (versus an apparent line width of 1200 Hz). This is a relatively long T_2' value for experiments carried out under DNP conditions (i.e. at cryogenic temperatures on a radical-doped sample), which can be explained by the following reasons: first and most importantly, the experiments were performed at fast MAS frequency (36 kHz) and under high power proton decoupling (125 kHz), which efficiently averages ^{1}H-^{13}C heteronuclear dipolar couplings; secondly, the relatively small pore diameter of the silica support largely prevents the TEKPol radical from penetrating the one-dimensional channel as demonstrated previously[57] and therefore little paramagnetic relaxation enhancement (PRE) effect is expected. All these factors jointly with the large values of the scalar couplings (see below) make the through-bond coherence transfer particularly efficient and, in combination with DNP signal enhancement factors of ~100, enable the acquisition with high-sensitivity of a full two-dimensional (2D) $^{13}C\{^{195}Pt\}$ *J*-HMQC correlation spectrum in 64 hours (Figure 2b). Quite unexpectedly, both the 1D and 2D $^{13}C\{^{195}Pt\}$ *J*-HMQC NMR spectra clearly evidence the presence of two distinct Pt-NHC sites, labelled (I) and (II).

The 2D $^{13}C\{^{195}Pt\}$ *J*-HMQC spectrum was acquired by synchronizing the t_1 increment with the rotor period, which folds the spinning sidebands of each Pt site into a single peak, thus improving the sensitivity.[53, 58] However, as the ^{195}Pt CSA amplitude is much larger than the MAS frequency, ^{195}Pt peaks observed in the 2D NMR spectrum can correspond to either the center band or a spinning sideband. To unambiguously determine the ^{195}Pt isotropic chemical shifts of site (I) and (II), two *J*-HMQC experiments were performed at different MAS frequencies (36 and 40 kHz).[59] The resulting spectra are shown in Figure S6 in the SI. Values of -3920 and -3500 ppm were respectively determined for site (I) and (II). The difference between these two ^{195}Pt δ_{iso} values is ca. 36 kHz, which rationalizes the fact that the two ^{195}Pt peaks appear roughly at the same chemical shift position in the spectrum of Figure 2b (bottom). Thus, in this spectrum, the correlation peak of site (I) corresponds to the center band, while that of site (II) is the first spinning sideband.

Solution NMR spectroscopy studies on molecular complexes have demonstrated that both the δ_{iso} of ^{13}C nuclei coordinating the Pt center and the one-bond scalar coupling $^{1}J(^{13}C\text{-}^{195}Pt)$ are sensitive structural reporters that can be used to probe the nature of the ligand in *trans* position of Pt-NHC complex.[60] The 1D and 2D *J*-HMQC spectra provide direct access to the ^{13}C δ_{iso}, which can be measured from the center of the doublet. Values of 178 and 153 ppm were obtained for site (I) and (II), respectively. The $^{1}J(^{13}C\text{-}^{195}Pt)$ values can be estimated by measuring the splitting in these doublets. However, the inhomogeneous broadening of the ^{13}C NMR spectra makes it difficult to accurately measure the $^{1}J(^{13}C\text{-}^{195}Pt)$ values from the observed splittings. Alternatively, and more accurately, $^{1}J(^{13}C\text{-}^{195}Pt)$ values can be determined from the modulation of the ^{13}C signal intensity in a series of 1D $^{13}C\{^{195}Pt\}$ *J*-HMQC spectra with varied τ_J times. The raw spectra are presented in Figure S7 in the SI. Figures 3a and b show the experimental points for site (I) and (II) as black dots, respectively. The two curves are expected to exhibit a sine squared modulation, from which the coupling values can be selectively extracted. Values of respectively 1670 ± 200 and 1395 ± 100 Hz were obtained for site (I) and (II). A larger deviation is observed for site (I), probably due to a wider distribution of values.

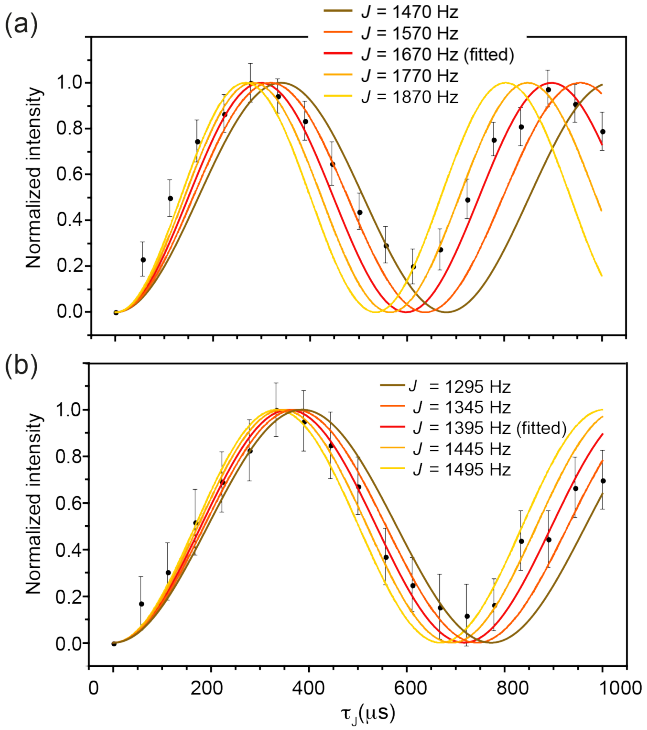

Figure 3. The *J*-modulation curves obtained from 1D $^{13}C\{^{195}Pt\}$ *J*-HMQC spectra as a function of τ_J for (a) the C6'(I) and (b) C6'(II) resonances. The experimental points are shown as black dots, while the coloured curves represent calculated curves with various $^1J(^{13}C\text{-}^{195}Pt)$ coupling values. The curves were calculated with a sine squared function, without taking into account transverse attenuation.

We then turned our attention to the measurement of the ^{195}Pt chemical shift (CS) tensor parameters, i.e., the δ_{iso}, the span (Ω), and skew (κ). These parameters are very sensitive to the Pt coordination sphere and could be used to refine the structures of these two sites. These tensor parameters are defined as follows:

$$\delta_{iso} = (\delta_{11} + \delta_{22} + \delta_{33})/3 \quad (1)$$

$$\Omega = \delta_{11} - \delta_{33} \quad (\Omega \geq 0) \quad (2)$$

$$\kappa = 3(\delta_{11} - \delta_{iso})/\Omega \quad (-1 \leq \kappa \leq 1) \quad (3)$$

where $\delta_{11} \geq \delta_{22} \geq \delta_{33}$ are the principal components of the CS tensor in the IUPAC convention.[61]

The ^{195}Pt δ_{iso} values have been already determined from rotor-synchronized $^{13}C\{^{195}Pt\}$ *J*-HMQC experiments as discussed above, leaving only Ω and κ to be determined. These two parameters can be extracted by fitting the CSA spinning sideband manifold pattern. In order to obtain this pattern, a series of $^{13}C\{^{195}Pt\}$ sideband-selective *J*-resolved experiments was performed. This experiment was originally proposed by Venkatesh et al to measure the ^{195}Pt CSA pattern with indirect proton or phosphorous detection.[53] Here, the sensitivity boost provided by DNP enabled the implementation of a ^{13}C detected *J*-resolved experiment. The corresponding pulse sequence is shown in Figure S3. In this experiment, a selective saturation pulse of weak radio-frequency B_1 field (here, 14 kHz) was applied on ^{195}Pt channel. The duration of the ^{195}Pt pulse was 55.6 ms (2 rotor cycles). When the carrier frequency of this pulse hits one of the spinning sidebands, the magnetization of the ^{13}C spins that are *J*-coupled to a neighboring ^{195}Pt spin will be reduced (not fully refocused). The intensity of the ^{13}C resonance will attenuated by a factor proportional to the intensity of the spinning sideband. By moving the carrier frequency of the ^{195}Pt pulse and observing the corresponding ^{13}C peak intensity reduction, the ^{195}Pt CSA spinning sideband manifold was thus traced out (Figure 4). As pointed out above, the ^{195}Pt δ_{iso} values for site (I) and (II) differ by ca. 36 kHz. As a consequence, the ^{195}Pt CSA spinning sideband positions of these two Pt sites can be acquired simultaneously by performing a single series of $^{13}C\{^{195}Pt\}$ sideband selective *J*-resolved experiments. In practice, starting from the isotropic shift, the carrier frequency of the sideband selective pulse was moved by steps of the MAS rate, so as to record the full ^{195}Pt CSA spinning sideband manifold. The experimental results as well as the result of the fits are shown in Figures 4a and b for site (I) and (II), respectively. Excellent fits are achieved for both sites. The extracted CSA parameter values are (Ω, κ) = (4550 ± 110 ppm, -0.53 ± 0.04) for site (I) and (Ω, κ) = (5950 ± 90 ppm, -0.65 ± 0.04) for site (II). The significantly different CSA parameters further confirm that they have different coordination environments. Table 1 summarizes the NMR parameters of these two Pt-NHC sites.

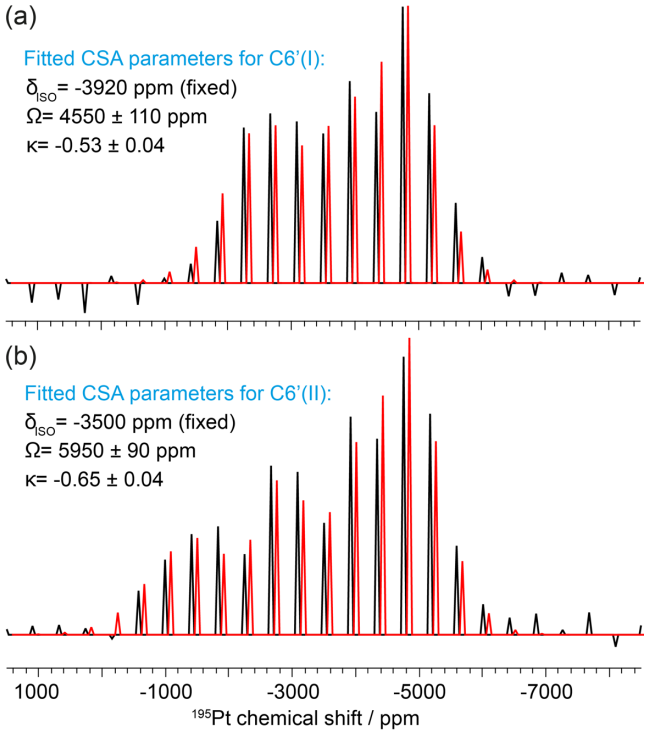

Figure 4. The ^{195}Pt spinning sideband manifolds measured with a series of $^{13}C\{^{195}Pt\}$ sideband selective *J*-resolved NMR experiments (in black) superimposed with the best-fit spectra (in red) for (a) the C6'(I) and (b) the C6'(II) resonances, respectively.

Table 1. Experimentally determined NMR parameters of the two Pt-NHC sites.

Site	δ_{iso} ^{13}C (ppm)	$^1J(^{13}C\text{-}^{195}Pt)$ (Hz)	δ_{iso} ^{195}Pt (ppm)	Ω ^{195}Pt (ppm)	κ ^{195}Pt
(I)	178	1670±200	-3920	4550±110	-0.53±0.04
(II)	154	1395±100	-3500	5950±90	-0.65±0.04

In summary, $^{13}C\{^{195}Pt\}$ *J*-HMQC and sideband-selective *J*-resolved experiments carried out under DNP conditions and in a fast MAS regime enabled the measurement of a set of five NMR parameters, namely the δ_{iso} ^{13}C, the $^1J(^{13}C\text{-}^{195}Pt)$ and the ^{195}Pt CS tensor parameters (δ_{iso} ^{195}Pt, Ω ^{195}Pt and κ ^{195}Pt) of the two Pt-NHC complexes,

providing direct and unique information on the Pt coordination spheres. It should be emphasized that, given the ca. 3 wt% Pt loading of **Pt(NHC)@SiO₂**, the experiments described above are only feasible with the combination of DNP with fast MAS and high power proton decoupling. Notably, the enhancement provided by DNP allowed one to detect the ^{195}Pt NMR signature indirectly on a low-γ nucleus directly bonded to the platinum, thereby extending the scope of the approach recently implemented by us to observe this signature by proton-detected room temperature solid-state NMR.

DFT studies on library of potential surface sites. In order to interpret these NMR parameters and propose specific structures for site (I) and (II), DFT calculations were performed on an extensive library of molecular Pt-NHC complexes to provide on the one hand calculated NMR signatures for a range of possible structures and on the other hand a general understanding on how various structural factors in square planar Pt(II)-NHC complexes influence the NMR signatures of the central ^{195}Pt nucleus and the coordinating ^{13}C atom (C6') of the NHC ligand. This eventually allows for the conversion of the experimental NMR data into structural pictures with a determination of the coordination environment of Pt-sites.

Potential candidates were chosen taking into account various grafting mechanisms of $[Pt(COD)Cl_2]$ on **NHC@SiO₂** and ligand exchange within the system. Since the bidentate COD ligand might be preserved upon grafting, the mono- and bis-grafted cationic species $[Pt(NHC)(COD)(Cl)]^+$ (**B1**) and $[Pt(NHC)_2(COD)]^{2+}$ (**B2**) were included into the library. Opening or complete loss of COD is explored in the other structures of the library which are of type $[Pt(Cl)(NHC)(L_t)(L_c)]$, L_t being the ligand trans and L_c the ligand cis to the NHC, respectively. We will refer to these structures using a two-letter code of type **xn** where x = 1-9 indicates L_t and n = a-e refers to L_c. For L_t we considered a second NHC ligand both in neutral and protonated forms, chloride and hydroxide ions, monodentate COD, a vacant site, $OSiF_3^-$ and $F_3Si\text{-}O\text{-}Si(CH_3)_3$ to mimic potential interactions between Pt and silica surface, as well as $OC(CF_3)_3^-$ to explore Pt-organic residue interactions. For L_c a subset of these ligands, namely chloride, monodentate COD, a second NHC, as well as $OSiF_3^-$ and $F_3Si\text{-}O\text{-}Si(CH_3)_3$ were taken into account. In the following graphic representations, different combinations of L_t and L_c are also labeled via a color-shape code. A schematic visualization of these two types of codes is provided in Figure 1b. To assist the reader to easily find the corresponding structure from the two-letter code or the color-shape code, a matrix table (Table S2 in the SI) is provided in which all structures are explicitly drawn. A complete list of all compounds that were evaluated and DFT results can be found from Table S3 in the SI.

Converting experimental NMR data into structural information. With the calculated NMR signatures of the library of potential structures in hands and the experimental NMR data for site (I) and (II), we next evaluated the possibility to solve their structures, by identifying the natures of the ligands bound to Pt. Figure 5a visually summarizes and presents the calculated and experimental NMR parameters in the form of barcodes. From left to right, the five columns display the values for δ_{iso} ^{13}C, $^1J(^{13}C\text{-}^{195}Pt)$, Ω ^{195}Pt, κ ^{195}Pt and δ_{iso} ^{195}Pt, respectively. From top to bottom, the first three rows respectively denote the model structures with $L_c = Cl^-$, COD or NHC; and, for each type of L_c, the structure with specific L_t is represented as a colored bar, where the color-coding is shown on the top of the figure (the same as the ones in Figure 1b). The special structures (**B1** and **B2**) for which the bidentate COD ligand is preserved are shown as brown bars in the fourth row, while the experimental values are reported using black and grey bars in last row (the uncertainty of the measurement being represented as the width of the bar). For a certain NMR signature, the best structure match can be simply found by searching for the bar that the most closely aligns with the experimental bar in the vertical direction. For example, considering δ_{iso} ^{13}C, the best match for site (II) is **6a** with $L_c = Cl^-$ and L_t = COD or **5b** with L_c = COD and $L_c = OC(CF_3)_3^-$. However, these two structures do not provide the best match for the other NMR parameters simultaneously. In order to find the structures in best agreement with the NMR data in an overall sense, a numerical comparison of the experimental parameters with the calculated values for all members of the DFT library was performed in two ways.

To determine the most representative model, we first calculated a simple metric or root-mean square deviation Σ defined as follows:

$$\Sigma = \left\{ \left[\frac{\left(\delta_{iso}^{13C}\right)_{exp} - \left(\delta_{iso}^{13C}\right)_{DFT}}{\Delta_{\left(\delta_{iso}^{13C}\right)_{DFT}}} \right]^2 + \left[\frac{\left(\delta_{iso}^{195Pt}\right)_{exp} - \left(\delta_{iso}^{195Pt}\right)_{DFT}}{\Delta_{\left(\delta_{iso}^{195Pt}\right)_{DFT}}} \right]^2 + \left[\frac{\left(\Omega^{195Pt}\right)_{exp} - \left(\Omega^{195Pt}\right)_{DFT}}{\Delta_{\left(\Omega^{195Pt}\right)_{DFT}}} \right]^2 + \left[\frac{\left(\kappa^{195Pt}\right)_{exp} - \left(\kappa^{195Pt}\right)_{DFT}}{\Delta_{\left(\kappa^{195Pt}\right)_{DFT}}} \right]^2 + \left[\frac{(J_{C-Pt})_{exp} - (J_{C-Pt})_{DFT}}{\Delta_{(J_{C-Pt})_{DFT}}} \right]^2 \right\}^{\frac{1}{2}} \quad (4)$$

where Δ are the standard deviations of the calculated parameters. The details and rationale for the calculation of Σ are presented in the SI. Figure 5b shows the ranking of the Σ values calculated for the 27 molecular models. These molecular models are arranged from left to right with increasing Σ value. The smaller the Σ value the better the match is between the model structure and experimental data, while close Σ values correspond to models with the same likelihood of being the correct structure. The blue and red bars correspond to molecular structures with one and two NHC ligands around the Pt metal center, respectively. The reason for this distinction will be clear in the following discussion.

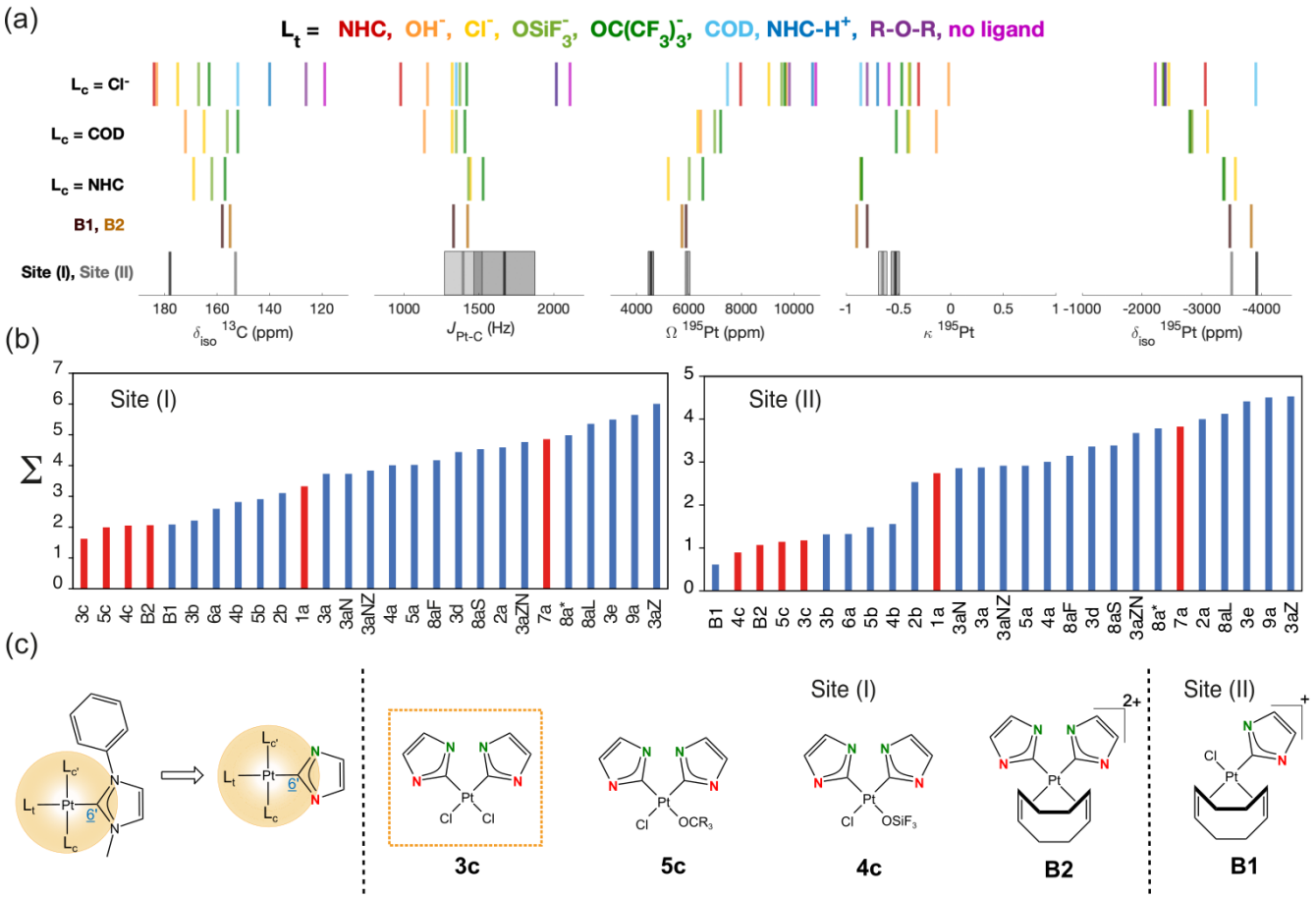

Figure 5. (a) "Barcode" representation of all evaluated NMR parameters; columns show from left to right: δ_{iso} ^{13}C, $^{1}J(^{13}C\text{-}^{195}Pt)$, Ω ^{195}Pt, κ ^{195}Pt and δ_{iso} ^{195}Pt. The upper three rows show calculated values for compounds of type **xn** with L_c = Cl^-, COD and NHC respectively, while **B1** and **B2** are shown in the fourth row and the experimental data for site (I) and (II) in the fifth row. (b) Plot of the root-mean square deviation Σ as defined in the main text for the 27 molecular models. The red bars correspond to bis-NHC structures. (c) Most probable structural assignments for sites (I) and (II) based on the comparison between the experimental data and the DFT library of molecular model compounds. In the molecular models the two nitrogen atoms are bonded to a phenyl and a methyl group as represented in the left-hand side of the figure.

Here, we would like to emphasize that our method aims at finding a structure simultaneously satisfying various (correlated) NMR signatures as a whole, while to our best knowledge, previous studies relied on a single NMR interaction.[39, 53] Using this approach, we can propose that the best fit for site (I) corresponds to the molecular model **3c**, *cis*-$[Pt(NHC)_2(Cl)_2]$, while it is **B1**, $[Pt(NHC)(Cl)(COD)]^+$ for site (II) (Figure 5c). Alternatively, a second approach was used to compare the experimentally extracted NMR parameters with the values calculated for all members of the DFT library. For each of the twenty-seven molecular models, we computed the difference between the experimental and calculated values of δ_{iso} ^{13}C, δ_{iso} ^{195}Pt, Ω ^{195}Pt, κ ^{195}Pt and $^{1}J(^{13}C\text{-}^{195}Pt)$. The models were then ranked for each NMR parameter, from 1 to 27, in the order of increasing magnitude. The sum of the ranking numbers over the 5 parameters arranges the models in a such a way that the structure with the lowest value corresponds to the best model. This ranking method leads to the same molecular models as the first approach, namely **3c** for site (I) and **B1** for site (II) (See Figures S10 and S11 in the SI).

In order to further confirm the assignment of site (I) to a bis-NHC platinum complexes, a one-dimensional dipolar-based ^{13}C double-quantum-filtered (DQF) experiment was recorded (see Figure 6). The ^{13}C resonance of C6′(I) was clearly observed in the spectrum. This suggests a close proximity between two carbon-13 labelled spins in the coordination sphere of site (I), thus corroborating its assignment to a structure where the Pt is surrounded by two NHC ligands. To our best knowledge, such a structure had never been observed before on surfaces. The absence of the C6′(II) resonance is in agreement with the proposed coordination sphere for the second site. The coordination with Cl^- ligands also agrees with EXAFS measurement in previous study.[40]

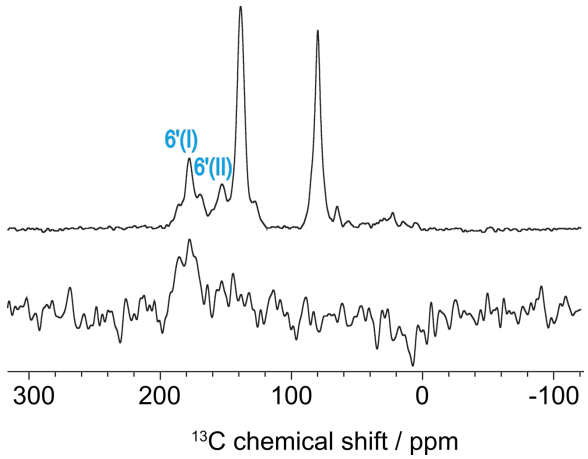

Figure 6. 1D ^{13}C CPMAS spectrum (top) and 1D dipolar double-quantum-filtered (DQF) ^{13}C spectrum acquired with BABA-xy16 pulse sequence for **Pt(NHC)@SiO$_2$**.

For site (I), other model structures with two NHC ligands that are in close agreement with the experimental data, namely **5c**, **4c** and **B2** could also be considered (Figures 5b and c). However, **5c** and **4c** are not compatible with the acquired NMR data since their C6' atoms are not chemically equivalent and should therefore reveal two distinct ^{13}C resonances. In contrast, for site (II) for which the experimental data point toward a single NHC ligand, model **B1** corresponds to the most probable structure. These proposed assignments indicate that grafting of $[Pt(COD)(Cl)_2]$ on **NHC@SiO₂** occurs partially via opening and successive replacement of the COD ligand by a second NHC ligand and partially upon loss of one Cl^-, retaining the bidentate COD ligand.

Understanding the relation between structure and NMR signatures. Next, with this data set in hands, we decided to understand the relation of these NMR signatures and the various structures. We first discuss the effect of *trans* and *cis* ligands on the individual NMR parameters.

Influence of L_t ligand on ^{13}C NMR parameters. In a first step we focus our analysis on the ^{13}C–based NMR parameters, i.e., the δ_{iso} of C6' and its scalar coupling with Pt (Figure 7a). The paramagnetic deshielding of the coordinating ^{13}C atom of NHC ligands in square planar Pt(II) complexes with the NHC being twisted out of plane is mainly driven by the most deshielded component δ_{11} ^{13}C which is oriented orthogonal to the metal-ligand plane.[53, 62] Since the paramagnetic terms dominate the overall chemical shielding of ^{13}C, δ_{11} ^{13}C also directs δ_{iso} ^{13}C. The high value of δ_{11} ^{13}C indicates that a pair of occupied and empty orbitals, close in energy and orthogonal to each other, must be present orthogonal to it, namely the Pt-NHC σ-bonding orbital with the Pt-NHC π*-antibonding orbital, that is associated with the empty orbital of the NHC carbene, a weak π-acceptor ligand (Figure 7c). Consequently, δ_{11} ^{13}C is determined by the strength of the Pt-NHC interaction: a weak Pt-NHC bond and therefore low energy gap between the bonding and antibonding orbitals result in very efficient deshielding and high values for δ_{11} ^{13}C and δ_{iso} ^{13}C, while the opposite holds in the case of strong Pt-NHC bond. Since the strength of the Pt-NHC bond is mainly influenced by the nature of the ligand *trans* to the NHC (L_t), δ_{iso} ^{13}C encodes information on the nature of L_t. Stronger σ-donors such as a second NHC ligand or an anionic X-type ligand (e.g. L_t = Cl^- or OH^-) weaken the Pt-NHC bond and increase δ_{iso} ^{13}C, while with weaker donors such as a neutral siloxane bridge mimic, a protonated NHC or in the absence of any ligand, a rather strong Pt-NHC bond and low δ_{iso} ^{13}C are present.

The scalar coupling $^1J(^{13}C\text{-}^{195}Pt)$ also encodes the strength of the Pt-NHC bond and therefore reports on the nature of L_t; the shorter the Pt-NHC bond, the larger the coupling $^1J(^{13}C\text{-}^{195}Pt)$. Since δ_{iso} ^{13}C and $^1J(^{13}C\text{-}^{195}Pt)$ are essentially driven by similar structural effects, a correlation exists between the two quantities, as illustrated in Figure 7a. This 2D representation of δ_{iso} ^{13}C and $^1J(^{13}C\text{-}^{195}Pt)$ across the entire library of molecular models clearly demonstrates that both parameters are dominated by the nature of L_t, while L_c plays only a marginal role, inducing only small variations of δ_{iso} ^{13}C and even less pronounced changes of $^1J(^{13}C\text{-}^{195}Pt)$.

In summary, the analysis of ^{13}C NMR data would be enough to draw key conclusions on the nature of L_t but does not provide sufficient information to differentiate between various possibilities for L_c. Consistent with our finding, based on δ_{iso} ^{13}C and $^1J(^{13}C\text{-}^{195}Pt)$ alone, this analysis indicates that site (I) should bear a strong σ-donor ligand in trans position. If such structures had been present for site (II), weaker donors would have been expected, e.g., COD (mono- or bidentate), $OSiF_3^-$ or $F_3Si\text{-}O\text{-}Si(CH_3)_3$, with the latter two being representative of potential interactions with surface siloxide groups. We note that, while site (II) lies on the line representing the linear relation between δ_{iso} ^{13}C and $^1J(^{13}C\text{-}^{195}Pt)$ for the DFT data, site (I) deviates from this relation and possesses a higher $^1J(^{13}C\text{-}^{195}Pt)$ than one would expect based on the measured δ_{iso} ^{13}C. This potentially points to the presence of specific effects related to the coordination environment of surface species (constrained positioning of surface ligands, e.g., orientation of the NHC ligand(s) with respect to the molecular plane), not captured by our molecular models for site (I) where all ligands bound to Pt can fully be relaxed (Figure 5a and vide infra for discussion).

Influence of L_c ligand on ^{195}Pt NMR parameters. We next examine the effect to L_c on the CS tensor parameters of the ^{195}Pt central atom. Due to the large CSA of ^{195}Pt, the span (Ω ^{195}Pt) and skew (κ ^{195}Pt) values (defined in equations (2) and (3) respectively) are valuable descriptors. As κ is a ratio and thus very sensitive to small structural variations, we focus on Ω and δ_{iso} ^{195}Pt as the most reliable source of structural information upon this set of available parameters. First, we incorporate Ω ^{195}Pt as a third dimension of information in addition to δ_{iso} ^{13}C and $^1J(^{13}C\text{-}^{195}Pt)$ (Figure 7b). Systematic variations in Ω ^{195}Pt are mostly driven by δ_{11}, the principal component of the ^{195}Pt CS tensor which is oriented orthogonal to the metal-ligand plane. The deshielding of δ_{11} results from the coupling of the Pt-L_n (where L_n represents all ligands) σ-bonding orbital to the Pt-L_n π*-antibonding orbital of all four ligands as visualized in Figure 7d. Note that one can also visualize this situation using the frontier molecular orbital picture for a d^8 square planar complex in which the HOMO $d_{(x2-y2)}$ and the LUMO $d_{(xy)}$ can be identified as the pair of orbitals which dominates. Since all ligands contribute to this pair of orbitals to a similar extent, L_c influences the ^{195}Pt δ_{11} and Ω to a similar extent as L_t. The Ω is reduced when δ_{11} becomes less deshielded, i.e., when the energy gap between Pt-L_n σ and Pt-L_n π* increases. This is induced by strong σ-donors which lower the Pt-L_n σ-bonding orbital energy or strong π-acceptors which raise the energy of the Pt-L_n π*-antibonding orbital. For molecular models containing a simple σ-donor ligand in *cis*-position such as Cl^-, OH^- or $OSiF_3^-$ we obtain spans above 8000 ppm which would have been far too high to match experimental values of site (I) and (II). Only when a π-acceptor such as a COD ligand (mono- or bidentate) or a second NHC is part of the ligand set, the span is significantly reduced to values ranging between 4000 and 7000 ppm (Figure 7c) which are comparable to the experimentally observed values. As δ_{11} also dominates δ_{iso} ^{195}Pt, this decrease in Ω is accompanied by a decrease of the δ_{iso}. This analysis further supports the presence of π-acceptor ligands in the *cis*-position to the NHC.

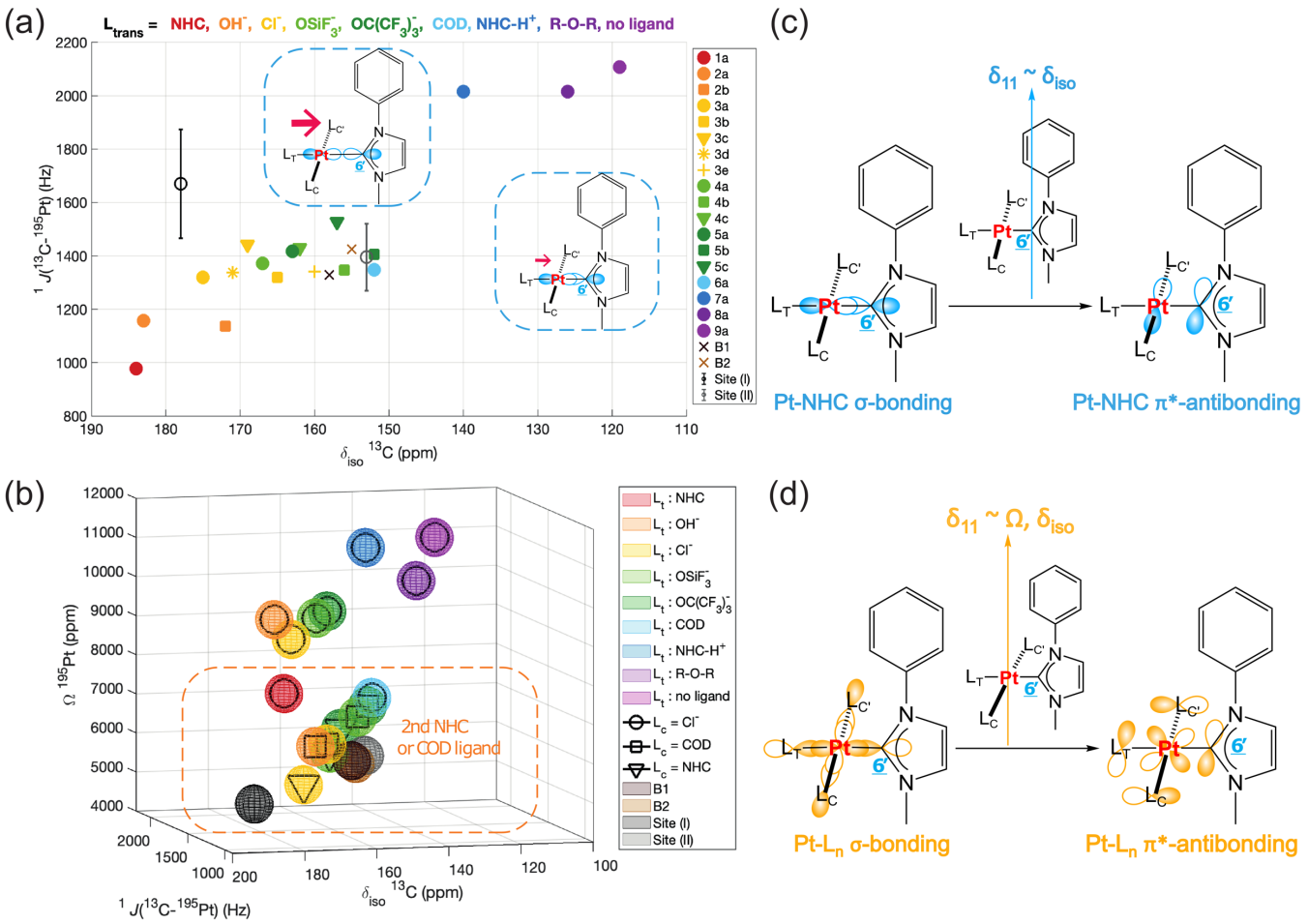

Figure 7. (a) Analysis of DFT calculated ^{13}C–based NMR parameters reveals a correlation between the isotropic chemical shift of the NHC C6' atom, δ_{iso} ^{13}C (in ppm), and the one-bond scalar coupling to the central Pt atom, $^{1}J(^{13}C\text{-}^{195}Pt)$ (in Hz). For calculated data points of type **xn**, the nature of L_t is encoded in the color while L_c is encoded in the shape of the individual points. Molecular models **B1** and **B2** are indicated as brown crosses, while experimental data for sites (I) and (II) are indicated in black and grey, with error bars for the *J* coupling values. As indicated by the schematic drawings in the dashed boxes strong ligands L_t decrease the Pt-NHC bonding strength while for relatively weak L_t a strong Pt-NHC bond is present. As both ^{13}C–based NMR parameters depend strongly on the Pt-NHC bonding strength, they mainly encode the nature of L_t whose σ-donation strength determines the position of the structures along the δ_{iso} ^{13}C- $^{1}J(^{13}C\text{-}^{195}Pt)$ line. Structures with same L_t but different L_c cluster together in this two-dimensional representation and are not distinguishable based on ^{13}C NMR parameters. (b) Three-dimensional representation including in addition to ^{13}C δ_{iso} (in ppm) and $^{1}J(^{13}C\text{-}^{195}Pt)$ (in Hz) also Ω ^{195}Pt (in ppm). Note that, even though included in our DFT library, compounds with other L_c than Cl^-, COD or NHC are not included in this representation. Structures with same L_t but different L_c are spread along the Ω ^{195}Pt dimension. The dashed orange box encloses all structures which contain either a second NHC or a COD ligand (mono- or bidentate) and both experimental data points. Only these structures show Ω ^{195}Pt below 7000 ppm as in addition to strong σ-donating ligands, π-accepting ligands are required to significantly lower Ω ^{195}Pt. (c) The most deshielded component of the ^{13}C CS tensor, δ_{11} ^{13}C, which dominates δ_{iso} ^{13}C reflects the coupling of the Pt-NHC σ-bonding with the Pt-NHC π*-antibonding orbitals, resulting in a strong dependence of δ_{iso} ^{13}C on the Pt-NHC bonding strength and thus the nature of L_t. d) The most deshielded component of the ^{195}Pt CS tensor, δ_{11}, which dominates Ω ^{195}Pt, reflects the coupling of the Pt-L_n σ-bonding with the Pt-L_n π*-antibonding orbitals and is thus sensitive to the nature of all four ligands.

Influence of NHC orientations. Of course, molecular models and actual surface structures may differ, e.g., due to constrains arising at the surface, namely arrangement of ligands that may not be readily accessible in molecular chemistry that can result in discrepancies between calculated and experimental NMR parameters. Since the highly directive Pt-NHC π-interaction is especially sensitive to geometric changes that alter the overlap of the respective *p* or *d*-type orbitals, the exact orientation of the NHC ligand with respect to the metal-ligand plane of the square planar structure is expected to have a significant influence on the NMR parameters. To evaluate the influence of the NHC orientation, we calculated NMR parameters for structural variants of **3a** where the NHC ligand was stepwise turned away from its orthogonal orientation (**3aN**) which was obtained upon geometry optimization into a parallel position with respect to the metal-ligand plane (**3aZ**). Although this structure (**3aZ**) is energetically unfavorable, it still provides an estimate of the largest shift of NMR parameters that may be induced by variations of the NHC orientation. Since turning the NHC ligand in-plane simultaneously positions the empty orbital of the NHC carbene out-of-plane (see Figure S9 in the SI), thereby weakening the π-interaction with the $d_{(xy)}$ orbital of the Pt atom, this geometric change is accompanied by a shielding of δ_{iso} ^{13}C from 175 to 123 ppm, an increase of Ω ^{195}Pt from 9048 ppm to 19964 ppm as well as an increase of δ_{iso} ^{195}Pt from –2446 to –1892 ppm. As $^{1}J(^{13}C\text{-}^{195}Pt)$ depends primarily on electron density in s-orbitals it is less affected than the other NMR parameters and is only decreased slightly from 1320 Hz to 1240 Hz. Our

molecular models are thus providing upper boundaries of δ_{iso} ^{13}C and $^{1}J(^{13}C\text{-}^{195}Pt)$ and lower boundaries of Ω ^{195}Pt and δ_{iso} ^{195}Pt for surface structures with similar ligand combinations.

Moreover, these findings have important implications for the structural analysis of site (I), that has the best match with structure **3c** and is therefore interpreted as a structure with two NHC ligands *cis* to each other. The strong dependence of δ_{iso} ^{13}C on the NHC orientation allows us to determine the relative orientation of these NHC ligands. Since the NMR data reveal only a single δ_{iso} ^{13}C resonance for site (I), the two NHC ligands have to be parallel to each other. In any non-parallel orientation, the ^{13}C atoms of the NHC ligands are chemically inequivalent and two distinct resonances would be observed in the NMR spectrum. To demonstrate this finding, we have calculated NMR parameters for a structural variant of **3c** in which one of the two NHC ligands has been turned into a parallel position with respect to the metal-ligand plane such that the NHC ligands stand orthogonal to each other (**3cZ**). As expected, this results in a shielding of δ_{iso} ^{13}C of the in-plane NHC ligand. In addition, δ_{iso} ^{13}C of the second NHC ligand that has remained in an out-of-plane orientation is deshielded compared to **3c**. Since they are competing π-acceptors, the ^{13}C NMR parameters of a NHC ligand also depend on the orientations of all the other NHC ligands in structures with more than one NHC ligand, rendering the analysis more complex than in models with only one NHC ligand.

Thus, the NMR signatures of site (I), which has the best match with structure **3a** with two NHC ligands *cis* to each other, indicate that these two ligands are likely not both perpendicular to the plane of the Pt(II) complex as expected in a molecular complex, but rather twisted, probably because of the constraint imposed by the relative positions of these two ligands attached at the surface of the material.

CONCLUSION

In this work, we showcase how DNP enhanced ^{195}Pt solid-state NMR spectroscopy under fast MAS along with multi-dimensional NMR (^{13}C-detected 1D and 2D ^{13}C-^{195}Pt *J*-HMQC as well as 1D sideband-selective *J*-resolved experiments) allows one to identify the presence of two surface sites, here in a silica-supported Pt-NHC material with distinct NMR signatures, and to gather complementary NMR parameters (^{13}C δ_{iso}, ^{195}Pt δ_{iso}, ^{195}Pt Ω, ^{195}Pt κ, $^{1}J(^{13}C\text{-}^{195}Pt)$) in a site-resolved way. DFT calculations of these NMR parameters on an extensive library of potential candidate molecular models enable to resolve the speciation and structures of these two surface sites and to unambiguously elucidate the natures and positions of the ligands coordinating the metal center on each site. This was possible by using a simple rank-based method or an average root-mean-square deviation representing the distance between the 5 pairs of experimental and calculated NMR parameters. We can thus propose that grafting a [(COD)PtCl$_2$] precursor onto a material containing NHC precursors yields two types of Pt sites: i) the sites (I) correspond best to Pt sites having two remaining chlorides along with two NHC ligands *cis* to each other and slightly twisted with respect to the molecular plane, and ii) the sites (II) correspond to a cationic Pt sites anchored to the surface by only one NHC, while conserving one Cl^- and the bidendate COD ligand, $[Pt(NHC)(Cl)(COD)]^+$. This study further illustrates the difference between molecular and surface chemistry of immobilized homogeneous catalysts, with the formation of mono- vs bis-grafted species, neutral and cationic species. This calls for caution when assigning surface structures based solely on what would be expected based on molecular chemistry knowledge.

Furthermore, we establish relationships between the NMR parameters and the natures and the positions of the various ligands, due to their high sensitivity to the local electronic structure. Notably we showed that both δ_{iso} ^{13}C and $^{1}J(^{13}C\text{-}^{195}Pt)$ are similarly dependent on the nature of the ligand in *trans* position to the NHC; strong σ-donor ligands weaken the Pt-NHC bond, while weak σ-donor ligands strengthen the bond, leading to respectively lower and higher values of the ^{13}C chemical shift and the scalar coupling. Furthermore, ^{195}Pt NMR parameters are required to identify the nature of the *cis* ligand with π-acceptor ligands yielding reduced Ω values. Overall, the complete set of five NMR parameters provides a spectral fingerprint encoding clues on the types and arrangement of the ligands.

Overall, the integrated approach introduced here represents a step forward in the atomic-level description of surface sites, even in the presence of multiple coexisting structures, here discussed with a prototypical Pt-NHC complexes. This study opens new avenues for exploiting the rich NMR spectral signatures of surface sites to resolve their speciation and structures.

EXPERIMENTAL SECTION

Synthesis of the materials. The synthesis of **Pt(NHC)@SiO$_2$** material is referred to the prior study.[40] Details regarding the synthesis of the ^{13}C labeled imidazolium precursor as well as infrared spectrum and elemental analysis of **Pt(NHC)@SiO$_2$** are given in the SI.

NMR Spectroscopy. For DNP enhanced solid-state NMR experiments, the sample was prepared by impregnating the powder material with a 16 mM solution of TEKPol[63] in 1,1,2,2-tetrachloroethane (TCE), and then packed into 1.3 mm zirconia rotor with Vespel caps. TEKPol was provided by Prof. Olivier Ouari (Aix-Marseille University). As the material is not air-sensitive, the preparation of the NMR sample was done at ambient condition. After packing, the rotor was inserted into the pre-cooled probe and span to the target MAS frequency.

The DNP enhanced solid-state NMR experiments were performed on a Bruker AVANCE III wide bore NMR spectrometer operating at 9.4 T equipped with a Bruker triple-resonance ^{1}H/X/Y 1.3-mm low-temperature (ca. 100 K) MAS probe and a Bruker 263 GHz gyrotron delivering continuous microwave (μw) irradiation to the sample through a corrugated waveguide. In order to carry out ^{13}C-^{195}Pt correlation experiments under DNP condition, the probe was configured to ^{1}H/^{13}C/^{195}Pt by using an insert made for ^{13}C/^{111}Cd (22 pF capacitor in parallel with 8-turn coil) without attaching any shunt capacitor on Y channel, removing the jumper to add serial capacitor into the probe circuit which increases the resonant frequencies of both X and Y channels and connecting a REDOR box (purchased at NMR Service, Germany) to the RF input port of X channel which splits the single resonant frequency into two frequencies. In this way, the frequency of Y channel can reach to ^{195}Pt (at a Larmor frequency of 86.06 MHz) and the relatively lower resonant frequency produced by the REDOR box on X channel can be tuned to ^{13}C (at a Larmor frequency of 100.66 MHz). This specific configuration method guarantees the highest possible RF efficiency on Y channel, so that ca. 200 kHz B_1 field can be generated on ^{195}Pt channel which is important for the correlation experiments. This configuration was used for all the DNP enhanced ssNMR experiments. The MAS rate, ν_R, was set to 36 or 40 kHz. The μw power was optimized to maximize the DNP enhancement factor ε_H, measured by comparing the proton signal intensities of the solvent with and without μw irradiation.

The 1D ^{13}C spectrum was obtained by performing $^{13}C\{^{1}H\}$ cross polarization MAS (CPMAS) experiment. The DNP build-up time constant, $T_{B,ON}$, was determined by fitting the polarization build-up curve obtained from $^{13}C\{^{1}H\}$ CPMAS based saturation recovery experiment. The recycle delay of experiments was set to $1.3\times T_{B,ON}$ to provide the optimal efficiency. The ^{13}C spin-spin relaxation time constant, T_2', was accessed by carrying out $^{13}C\{^{1}H\}$ CPMAS spin echo experiments with varied echo delays which were synchronized with rotor period. 1D and 2D through-bond $^{13}C\{^{195}Pt\}$ correlation NMR spectra were acquired using a *J*-coupling mediated heteronuclear multiple-quantum correlation (*J*-HMQC) pulse sequence. The multiplicity of NHC ligand was checked with 1D ^{13}C double-quantum filtered (DQF) spectrum using BaBa-xy16 pulse sequence.[64] 1D through-space $^{13}C\{^{195}Pt\}$ dipolar mediated HMQC (D-HMQC) experiment was also implemented with R^3 or $SR4_1^2$ dipolar recoupling sequence but with no success. The chemical shift (CS) tensor parameters of surface Pt sites were measured by implementing a through-bond $^{13}C\{^{195}Pt\}$ sideband selective *J*-resolved experiment. The resulting ^{195}Pt CSA spinning sideband manifolds were fitted using DMFIT[65] to extract the CSA parameters. To do the fitting with DMFIT, zero points were evenly inserted between experimental data points. The ^{13}C chemical shift was referenced with alanine CH peak at 52 ppm; and the ^{195}Pt chemical shift was calibrated based on ^{13}C reference frequency according to the IUPAC recommendation. The detailed experimental acquisition parameters are given in the SI. Alternatively, the experimental data were fitted using the SIMPSON software. The fitted values were close to those obtained with DMFIT (see Table S4 in the SI).

Computational modeling. To derive the surface Pt site structures in **Pt(NHC)@SiO₂**, DFT calculations were performed for an extensive library of possible molecular Pt-NHC complexes. To accelerate the structure optimization, a pre-optimization calculation of the rotamer for each model was carried out with CREST.[66] Geometry optimization calculations were then performed using Gaussian 09[67] program suite with the B3LYP[68] functional in combination with the lanl2dz[69] basis set plus an additional f depolarization function for Pt atom and the 6-311+g(d)[70] basis set for all the other atoms. NMR parameters were calculated using ADF 2019 code.[71-73] The hybrid PBE0 exchange functional[74, 75] was used in combined with the triple zeta basis set with one additional polarization function (TZP) for all atoms except for Pt, for which a quadruple zeta basis with four polarization functions (QZ4P) was made use of.[76] Relativistic effects were account for with the zero order regular approximation (ZORA) approach of ADF.[77-79] To calculate $^{1}J(^{13}C\text{-}^{195}Pt)$, the specialized ZORA/TZ2P-J and ZORA/QZ4P-J basis sets available in ADF were chosen for C and Pt atoms, respectively; whereas, the exchange correlation functional and basis sets for the other atoms used were the same as for calculating chemical shift tensor. In addition, Gaussian nucleus modelling was applied in conjunction with an improved integration grid quality in order to properly calculate the *J*-coupling as recommended in the ADF 2019 user manual.

ASSOCIATED CONTENT

Supporting Information

The Supporting Information is available free of charge on the ACS Publications website.

Detailed synthesis procedure, elemental analysis result and FTIR spectrum of the material, supplementary NMR experimental details, calculations and spectra, and supplementary illustration figures, results and analysis on the DFT calculations (PDF).

AUTHOR INFORMATION

Corresponding Authors

* anne.lesage@ens-lyon.fr
* ccoperet@ethz.ch
* arossini@iastate.edu

ACKNOWLEDGMENT

This work has been supported by the Common Research Laboratory CARMEN (ENS de Lyon, CNRS, IFPEN, Claude Bernard Lyon 1 University, Sorbonne University, and University of Strasbourg). This work is part of a project that has received funding from the European Union's Horizon 2020 research and innovation program under Grant Agreement No 101008500 ("PANACEA"). AJR acknowledges primary support from the National Science Foundation CBET-1916809 and additional support from the Alfred P. Sloan Foundation through a Sloan research fellowship.

REFERENCES

(1) Bellotti, P.; Koy, M.; Hopkinson, M. N.; Glorius, F. Recent Advances in the Chemistry and Applications of N-Heterocyclic Carbenes. *Nat. Rev. Chem.* **2021**, *5* (10), 711-725.

(2) Hopkinson, M. N.; Richter, C.; Schedler, M.; Glorius, F. An Overview of N-Heterocyclic Carbenes. *Nature* **2014**, *510* (7506), 485-496.

(3) Ranganath, K. V. S.; Onitsuka, S.; Kumar, A. K.; Inanaga, J. Recent Progress of N-Heterocyclic Carbenes in Heterogeneous Catalysis. *Catal. Sci. Technol.* **2013**, *3* (9), 2161-2181.

(4) Pucino, M.; Inoue, M.; Gordon, C. P.; Schowner, R.; Stohr, L.; Sen, S.; Hegedus, C.; Robe, E.; Toth, F.; Buchmeiser, M. R.; Coperet, C. Promoting Terminal Olefin Metathesis with a Supported Cationic Molybdenum Imido Alkylidene N-Heterocyclic Carbene Catalyst. *Angew. Chem. Int. Ed.* **2018**, *57* (44), 14566-14569.

(5) Smith, C. A.; Narouz, M. R.; Lummis, P. A.; Singh, I.; Nazemi, A.; Li, C. H.; Crudden, C. M. N-Heterocyclic Carbenes in Materials Chemistry. *Chem. Rev.* **2019**, *119* (8), 4986-5056.

(6) Koy, M.; Bellotti, P.; Das, M.; Glorius, F. N-Heterocyclic Carbenes as Tunable Ligands for Catalytic Metal Surfaces. *Nat. Catal.* **2021**, *4* (5), 352-363.

(7) Ranganath, K. V. S.; Kloesges, J.; Schafer, A. H.; Glorius, F. Asymmetric Nanocatalysis: N-Heterocyclic Carbenes as Chiral Modifiers of Fe3O4/Pd Nanoparticles. *Angew. Chem. Int. Ed.* **2010**, *49* (42), 7786-7789.

(8) Ernst, J. B.; Muratsugu, S.; Wang, F.; Tada, M.; Glorius, F. Tunable Heterogeneous Catalysis: N-Heterocyclic Carbenes as Ligands for Supported Heterogeneous Ru/K-Al2O3 Catalysts to Tune Reactivity and Selectivity. *J. Am. Chem. Soc.* **2016**, *138* (34), 10718-10721.

(9) Cao, Z.; Kim, D.; Hong, D. C.; Yu, Y.; Xu, J.; Lin, S.; Wen, X. D.; Nichols, E. M.; Jeong, K.; Reimer, J. A.; Yang, P. D.; Chang, C. J. A Molecular Surface Functionalization Approach to Tuning Nanoparticle Electrocatalysts for Carbon Dioxide Reduction. *J. Am. Chem. Soc.* **2016**, *138* (26), 8120-8125.

(10) Ernst, J. B.; Schwermann, C.; Yokota, G. I.; Tada, M.; Muratsugu, S.; Doltsinis, N. L.; Glorius, F. Molecular Adsorbates Switch on Heterogeneous Catalysis: Induction of Reactivity by N-Heterocyclic Carbenes. *J. Am. Chem. Soc.* **2017**, *139* (27), 9144-9147.

(11) Narouz, M. R.; Osten, K. M.; Unsworth, P. J.; Man, R. W. Y.; Salorinne, K.; Takano, S.; Tomihara, R.; Kaappa, S.; Malola, S.; Dinh, C. T.; Padmos, J. D.; Ayoo, K.; Garrett, P. J.; Nambo, M.; Horton, J. H.; Sargent, E. H.; Hakkinen, H.; Tsukuda, T.; Crudden, C. M. N-Heterocyclic Carbene-Functionalized Magic-Number Gold Nanoclusters. *Nat. Chem.* **2019**, *11* (5), 419-425.

(12) Kaeffer, N.; Mance, D.; Coperet, C. N-Heterocyclic Carbene Coordination to Surface Copper Sites in Selective Semihydrogenation

Catalysts from Solid-State NMR Spectroscopy. *Angew. Chem. Int. Ed.* **2020**, *59* (45), 19999-20007.
(13) Wu, C. Y.; Wolf, W. J.; Levartovsky, Y.; Bechtel, H. A.; Martin, M. C.; Toste, F. D.; Gross, E. High-Spatial-Resolution Mapping of Catalytic Reactions on Single Particles. *Nature* **2017**, *541* (7638), 511-515.
(14) Conley, M. P.; Coperet, C.; Thieuleux, C. Mesostructured Hybrid Organic-Silica Materials: Ideal Supports for Well-Defined Heterogeneous Organometallic Catalysts. *ACS Catal.* **2014**, *4* (5), 1458-1469.
(15) Cavailles, M.; Bornet, A.; Jaurand, X.; Vuichoud, B.; Baudouin, D.; Baudin, M.; Veyre, L.; Bodenhausen, G.; Dumez, J. N.; Jannin, S.; Coperet, C.; Thieuleux, C. Tailored Microstructured Hyperpolarizing Matrices for Optimal Magnetic Resonance Imaging. *Angew. Chem. Int. Ed.* **2018**, *57* (25), 7453-7457.
(16) Gajan, D.; Schwarzwalder, M.; Conley, M. P.; Gruning, W. R.; Rossini, A. J.; Zagdoun, A.; Lelli, M.; Yulikov, M.; Jeschke, G.; Sauvee, C.; Ouari, O.; Tordo, P.; Veyre, L.; Lesage, A.; Thieuleux, C.; Emsley, L.; Coperet, C. Solid-Phase Polarization Matrixes for Dynamic Nuclear Polarization from Homogeneously Distributed Radicals in Mesostructured Hybrid Silica Materials. *J. Am. Chem. Soc.* **2013**, *135* (41), 15459-15466.
(17) Maishal, T. K.; Alauzun, J.; Basset, J. M.; Coperet, C.; Corriu, R. J. P.; Jeanneau, E.; Mehdi, A.; Reye, C.; Veyre, L.; Thieuleux, C. A Tailored Organometallic-Inorganic Hybrid Mesostructured Material: A Route to a Well-Defined, Active, and Reusable Heterogeneous Iridium-NHC Catalyst for H/D Exchange. *Angew. Chem. Int. Ed.* **2008**, *47* (45), 8654-8656.
(18) Maishal, T. K.; Boualleg, M.; Bouhrara, M.; Coperet, C.; Jeanneau, E.; Veyre, L.; Thieuleux, C. Domination of Local Environment Over Pore Confinement Effects on the Catalytic Performances of Single-Site Cp*Ir-III-NHC Heterogeneous vs. Homogeneous H/D Exchange Catalysts. *Eur. J. Inorg. Chem.* **2010**, (31), 5005-5010.
(19) Engl, P. S.; Santiago, C. B.; Gordon, C. P.; Liao, W. C.; Fedorov, A.; Coperet, C.; Sigman, M. S.; Togni, A. Exploiting and Understanding the Selectivity of Ru-N-Heterocyclic Carbene Metathesis Catalysts for the Ethenolysis of Cyclic Olefins to alpha,omega-Dienes. *J. Am. Chem. Soc.* **2017**, *139* (37), 13117-13125.
(20) Cao, Z.; Derrick, J. S.; Xu, J.; Gao, R.; Gong, M.; Nichols, E. M.; Smith, P. T.; Liu, X. W.; Wen, X. D.; Coperet, C.; Chang, C. J. Chelating N-Heterocyclic Carbene Ligands Enable Tuning of Electrocatalytic CO2 Reduction to Formate and Carbon Monoxide: Surface Organometallic Chemistry. *Angew. Chem. Int. Ed.* **2018**, *57* (18), 4981-4985.
(21) Samantaray, M. K.; Alauzun, J.; Gajan, D.; Kavitake, S.; Mehdi, A.; Veyre, L.; Lelli, M.; Lesage, A.; Emsley, L.; Copéret, C.; Thieuleux, C. Evidence for Metal–Surface Interactions and Their Role in Stabilizing Well-Defined Immobilized Ru–NHC Alkene Metathesis Catalysts. *J. Am. Chem. Soc.* **2013**, *135* (8), 3193-3199.
(22) Jabbour, R.; Renom-Carrasco, M.; Chan, K. W.; Völker, L.; Berruyer, P.; Wang, Z.; Widdifield, C. M.; Lelli, M.; Gajan, D.; Copéret, C.; Thieuleux, C.; Lesage, A. Multiple Surface Site Three-Dimensional Structure Determination of a Supported Molecular Catalyst. *J. Am. Chem. Soc.* **2022**, *144* (23), 10270-10281.
(23) Copéret, C.; Liao, W.-C.; Gordon, C. P.; Ong, T.-C. Active Sites in Supported Single-Site Catalysts: An NMR Perspective. *J. Am. Chem. Soc.* **2017**, *139* (31), 10588-10596.
(24) Grekov, D.; Vancompernolle, T.; Taoufik, M.; Delevoye, L.; Gauvin, R. M. Solid-State NMR of Quadrupolar Nuclei for Investigations into Supported Organometallic Catalysts: Scope and Frontiers. *Chem. Soc. Rev.* **2018**, *47* (8), 2572-2590.
(25) Qi, G.; Wang, Q.; Xu, J.; Deng, F. Solid-State NMR Studies of Internuclear Correlations for Characterizing Catalytic Materials. *Chem. Soc. Rev.* **2021**, *50* (15), 8382-8399.
(26) Kobayashi, T.; Perras, F. A.; Slowing, I. I.; Sadow, A. D.; Pruski, M. Dynamic Nuclear Polarization Solid-State NMR in Heterogeneous Catalysis Research. *ACS Catal.* **2015**, *5* (12), 7055-7062.
(27) Liao, W. C.; Ghaffari, B.; Gordon, C. P.; Xu, J.; Coperet, C. Dynamic Nuclear Polarization Surface Enhanced NMR Spectroscopy (DNP SENS): Principles, Protocols, and Practice. *Curr. Opin. Colloid Interface Sci.* **2018**, *33*, 63-71.
(28) Berruyer, P.; Emsley, L.; Lesage, A. DNP in Materials Science: Touching the Surface. *eMagRes* **2018**, *7* (4), 93-104.
(29) Hooper, R. W.; Klein, B. A.; Michaelis, V. K. Dynamic Nuclear Polarization (DNP) 101: A New Era for Materials. *Chem. Mater.* **2020**, *32* (11), 4425-4430.
(30) Nagashima, H.; Trebosc, J.; Kon, Y.; Sato, K.; Lafon, O.; Amoureux, J.-P. Observation of Low-γ Quadrupolar Nuclei by Surface-Enhanced NMR Spectroscopy. *J. Am. Chem. Soc.* **2020**, *142* (24), 10659-10672.
(31) Lesage, A.; Lelli, M.; Gajan, D.; Caporini, M. A.; Vitzthum, V.; Mieville, P.; Alauzun, J.; Roussey, A.; Thieuleux, C.; Mehdi, A.; Bodenhausen, G.; Coperet, C.; Emsley, L. Surface Enhanced NMR Spectroscopy by Dynamic Nuclear Polarization. *J. Am. Chem. Soc.* **2010**, *132* (44), 15459-15461.
(32) Rossini, A. J.; Zagdoun, A.; Lelli, M.; Lesage, A.; Copéret, C.; Emsley, L. Dynamic Nuclear Polarization Surface Enhanced NMR Spectroscopy. *Acc. Chem. Res.* **2013**, *46* (9), 1942-1951.
(33) Gutmann, T.; Liu, J. Q.; Rothermel, N.; Xu, Y. P.; Jaumann, E.; Werner, M.; Breitzke, H.; Sigurdsson, S. T.; Buntkowsky, G. Natural Abundance N-15 NMR by Dynamic Nuclear Polarization: Fast Analysis of Binding Sites of a Novel Amine-Carboxyl-Linked Immobilized Dirhodium Catalyst. *Chem. Eur. J.* **2015**, *21* (9), 3798-3805.
(34) Ong, T.-C.; Liao, W.-C.; Mougel, V.; Gajan, D.; Lesage, A.; Emsley, L.; Copéret, C. Atomistic Description of Reaction Intermediates for Supported Metathesis Catalysts Enabled by DNP SENS. *Angew. Chem. Int. Ed.* **2016**, *55* (15), 4743-4747.
(35) Delley, M. F.; Lapadula, G.; Núñez-Zarur, F.; Comas-Vives, A.; Kalendra, V.; Jeschke, G.; Baabe, D.; Walter, M. D.; Rossini, A. J.; Lesage, A.; Emsley, L.; Maury, O.; Copéret, C. Local Structures and Heterogeneity of Silica-Supported M(III) Sites Evidenced by EPR, IR, NMR, and Luminescence Spectroscopies. *J. Am. Chem. Soc.* **2017**, *139* (26), 8855-8867.
(36) Perras, F. A.; Padmos, J. D.; Johnson, R. L.; Wang, L.-L.; Schwartz, T. J.; Kobayashi, T.; Horton, J. H.; Dumesic, J. A.; Shanks, B. H.; Johnson, D. D.; Pruski, M. Characterizing Substrate–Surface Interactions on Alumina-Supported Metal Catalysts by Dynamic Nuclear Polarization-Enhanced Double-Resonance NMR Spectroscopy. *J. Am. Chem. Soc.* **2017**, *139* (7), 2702-2709.
(37) Camacho-Bunquin, J.; Ferrandon, M.; Sohn, H.; Yang, D.; Liu, C.; Ignacio-de Leon, P. A.; Perras, F. A.; Pruski, M.; Stair, P. C.; Delferro, M. Chemoselective Hydrogenation with Supported Organoplatinum(IV) Catalyst on Zn(II)-Modified Silica. *J. Am. Chem. Soc.* **2018**, *140* (11), 3940-3951.
(38) Pump, E.; Bendjeriou-Sedjerari, A.; Viger-Gravel, J.; Gajan, D.; Scotto, B.; Samantaray, M. K.; Abou-Hamad, E.; Gurinov, A.; Almaksoud, W.; Cao, Z.; Lesage, A.; Cavallo, L.; Emsley, L.; Basset, J. M. Predicting the DNP-SENS Efficiency in Reactive Heterogeneous Catalysts from Hydrophilicity. *Chem. Sci.* **2018**, *9* (21), 4866-4872.
(39) Venkatesh, A.; Lund, A.; Rochlitz, L.; Jabbour, R.; Gordon, C. P.; Menzildjian, G.; Viger-Gravel, J.; Berruyer, P.; Gajan, D.; Copéret, C.; Lesage, A.; Rossini, A. J. The Structure of Molecular and Surface Platinum Sites Determined by DNP-SENS and Fast MAS 195Pt Solid-State NMR Spectroscopy. *J. Am. Chem. Soc.* **2020**, *142* (44), 18936-18945.
(40) Berruyer, P.; Lelli, M.; Conley, M. P.; Silverio, D. L.; Widdifield, C. M.; Siddiqi, G.; Gajan, D.; Lesage, A.; Copéret, C.; Emsley, L. Three-Dimensional Structure Determination of Surface Sites. *J. Am. Chem. Soc.* **2017**, *139* (2), 849-855.
(41) Conley, M. P.; Drost, R. M.; Baffert, M.; Gajan, D.; Elsevier, C.; Franks, W. T.; Oschkinat, H.; Veyre, L.; Zagdoun, A.; Rossini, A.; Lelli, M.; Lesage, A.; Casano, G.; Ouari, O.; Tordo, P.; Emsley, L.; Copéret, C.; Thieuleux, C. A Well-Defined Pd Hybrid Material for the Z-Selective Semihydrogenation of Alkynes Characterized at the Molecular Level by DNP SENS. *Chem. Eur. J.* **2013**, *19* (37), 12234-12238.
(42) Romanenko, I.; Gajan, D.; Sayah, R.; Crozet, D.; Jeanneau, E.; Lucas, C.; Leroux, L.; Veyre, L.; Lesage, A.; Emsley, L.; Lacote, E.; Thieuleux, C. Iridium(I)/N-Heterocyclic Carbene Hybrid Materials: Surface Stabilization of Low-Valent Iridium Species for High Catalytic Hydrogenation Performance. *Angew. Chem. Int. Ed.* **2015**, *54* (44), 12937-12941.
(43) Werghi, B.; Pump, E.; Tretiakov, M.; Abou-Hamad, E.; Gurinov, A.; Doggali, P.; Anjum, D. H.; Cavallo, L.; Bendjeriou-Sedjerari, A.; Basset, J. M. Exploiting the Interactions between the Ruthenium Hoveyda-Grubbs

Catalyst and Al-Modified Mesoporous Silica: The Case of SBA15 vs. KCC-1. *Chem. Sci.* **2018**, *9* (14), 3531-3537.
(44) Conley, M. P.; Rossini, A. J.; Comas-Vives, A.; Valla, M.; Casano, G.; Ouari, O.; Tordo, P.; Lesage, A.; Emsley, L.; Copéret, C. Silica-Surface Reorganization during Organotin Grafting Evidenced by 119Sn DNP SENS: A Tandem Reaction of Gem-Silanols and Strained Siloxane Bridges. *Phys. Chem. Chem. Phys.* **2014**, *16* (33), 17822-17827.
(45) Vancompernolle, T.; Trivelli, X.; Delevoye, L.; Pourpoint, F.; Gauvin, R. M. On the Use of Solid-State 45Sc NMR for Structural Investigations of Molecular and Silica-Supported Scandium Amide Catalysts. *Dalton Trans.* **2017**, *46* (39), 13176-13179.
(46) Mance, D.; Comas-Vives, A.; Coperet, C. Proton-Detected Multidimensional Solid-State NMR Enables Precise Characterization of Vanadium Surface Species at Natural Abundance. *J. Phys. Chem. Lett.* **2019**, *10* (24), 7898-7904.
(47) Culver, D. B.; Venkatesh, V.; Huynh, H.; Rossini, A. J.; Conley, M. P. Al(ORF)(3) (R-F = C(CF3)(3)) activated silica: a well-defined weakly coordinating surface anion. *Chem. Sci.* **2020**, *11* (6), 1510-1517.
(48) D'Elia, V.; Dong, H. L.; Rossini, A. J.; Widdifield, C. M.; Vummaleti, S. V. C.; Minenkov, Y.; Poater, A.; Abou-Hamad, E.; Pelletier, J. D. A.; Cavallo, L.; Emsley, L.; Basset, J. M. Cooperative Effect of Monopodal Silica-Supported Niobium Complex Pairs Enhancing Catalytic Cyclic Carbonate Production. *J. Am. Chem. Soc.* **2015**, *137* (24), 7728-7739.
(49) Eedugurala, N.; Wang, Z. R.; Yan, K. K.; Boteju, K. C.; Chaudhary, U.; Kobayashi, T.; Ellern, A.; Slowing, I. I.; Pruski, M.; Sadow, A. D. beta-SiH-Containing Tris(silazido) Rare-Earth Complexes as Homogeneous and Grafted Single-Site Catalyst Precursors for Hydroamination. *Organometallics* **2017**, *36* (6), 1142-1153.
(50) Ishizaka, Y.; Arai, N.; Matsumoto, K.; Nagashima, H.; Takeuchi, K.; Fukaya, N.; Yasuda, H.; Sato, K.; Choi, J. C. Bidentate Disilicate Framework for Bis-Grafted Surface Species. *Chem. Eur. J.* **2021**, *27* (47), 12069-12077.
(51) Love, A. M.; Cendejas, M. C.; Hanrahan, M. P.; Carnahan, S. L.; Uchupalanun, P.; Rossini, A. J.; Hermans, I. Understanding the Synthesis of Supported Vanadium Oxide Catalysts Using Chemical Grafting. *Chem. Eur. J.* **2020**, *26* (5), 1052-1063.
(52) Kobayashi, T.; Perras, F. A.; Goh, T. W.; Metz, T. L.; Huang, W.; Pruski, M. DNP-Enhanced Ultrawideline Solid-State NMR Spectroscopy: Studies of Platinum in Metal-Organic Frameworks. *J. Phys. Chem. Lett.* **2016**, *7* (13), 2322-2327.
(53) Venkatesh, A.; Gioffrè, D.; Atterberry, B. A.; Rochlitz, L.; Carnahan, S. L.; Wang, Z.; Menzildjian, G.; Lesage, A.; Copéret, C.; Rossini, A. J. Molecular and Electronic Structure of Isolated Platinum Sites Enabled by the Expedient Measurement of 195Pt Chemical Shift Anisotropy. *J. Am. Chem. Soc.* **2022**, *144* (30), 13511-13525.
(54) Alauzun, J.; Mehdi, A.; Rey, C.; Corriu, R. Direct Synthesis of Ordered Mesoporous Silica Containing Iodopropyl Groups. A Useful Function for Chemical Modifications. *New J. Chem.* **2007**, *31* (6), 911-915.
(55) Bax, A.; Summers, M. F. 1H and 13C Assignments from Sensitivity-Enhanced Detection of Heteronuclear Multiple-Bond Connectivity by 2D Multiple Quantum NMR. *J. Am. Chem. Soc.* **1986**, *108* (8), 2093-2094.
(56) Mandal, P. K.; Majumdar, A. A Comprehensive Discussion of HSQC and HMQC Pulse Sequences. *Concepts Magn. Reson.* **2004**, *20A* (1), 1-23.
(57) Pinon, A. C.; Schlagnitweit, J.; Berruyer, P.; Rossini, A. J.; Lelli, M.; Socie, E.; Tang, M.; Pham, T.; Lesage, A.; Schantz, S.; Emsley, L. Measuring Nano- to Microstructures from Relayed Dynamic Nuclear Polarization NMR. *J. Phys. Chem. C* **2017**, *121* (29), 15993-16005.
(58) Li, Y. X.; Trebosc, J.; Hu, B. W.; Shen, M.; Amoureux, J. P.; Lafon, O. Indirect Detection of Broad Spectra in Solid-State NMR Using Interleaved DANTE Trains. *J. Magn. Reson.* **2018**, *294*, 101-114.
(59) Paluch, P.; Rankin, A. G. M.; Trebosc, J.; Lafon, O.; Amoureux, J. P. Analysis of HMQC experiments applied to a spin 1/2 nucleus subject to very large CSA. *Solid State Nucl. Magn. Reson.* **2019**, *100*, 11-25.
(60) Cherwinski, W. J.; Johnson, B. F. G.; Lewis, J.; Norton, J. R. Carbon-13 Nuclear Magnetic Resonance Spectra of Some Carbon-13 Monoxide Derivatives of Platinum(II). *J. Chem. Soc., Dalton Trans.* **1975**, (12), 1156-1158.
(61) Mason, J. Conventions for the Reporting of Nuclear Magnetic Shielding (or Shift) Tensors Suggested by Participants in the Nato ARW on NMR Shielding Constants at the University of Maryland, College-Park July 1992. *Solid State Nucl. Magn. Reson.* **1993**, *2* (5), 285-288.
(62) Arduengo, A. J.; Dixon, D. A.; Kumashiro, K. K.; Lee, C.; Power, W. P.; Zilm, K. W. Chemical Shielding Tensor of a Carbene. *J. Am. Chem. Soc.* **1994**, *116* (14), 6361-6367.
(63) Zagdoun, A.; Casano, G.; Ouari, O.; Schwarzwalder, M.; Rossini, A. J.; Aussenac, F.; Yulikov, M.; Jeschke, G.; Copéret, C.; Lesage, A.; Tordo, P.; Emsley, L. Large Molecular Weight Nitroxide Biradicals Providing Efficient Dynamic Nuclear Polarization at Temperatures up to 200 K. *J. Am. Chem. Soc.* **2013**, *135* (34), 12790-12797.
(64) Saalwachter, K.; Lange, F.; Matyjaszewski, K.; Huang, C. F.; Graf, R. BaBa-xy16: Robust and Broadband Homonuclear DQ Recoupling for Applications in Rigid and Soft Solids up to the Highest MAS Frequencies. *J. Magn. Reson.* **2011**, *212* (1), 204-215.
(65) Massiot, D.; Fayon, F.; Capron, M.; King, I.; Le Calve, S.; Alonso, B.; Durand, J. O.; Bujoli, B.; Gan, Z. H.; Hoatson, G. Modelling One- and Two-Dimensional Solid-State NMR Spectra. *Magn. Reson. Chem.* **2002**, *40* (1), 70-76.
(66) Pracht, P.; Bohle, F.; Grimme, S. Automated Exploration of the Low-Energy Chemical Space with Fast Quantum Chemical Methods. *Phys. Chem. Chem. Phys.* **2020**, *22* (14), 7169-7192.
(67) Frisch, M. J.; Trucks, G. W.; Schlegel, H. B.; Scuseria, G. E.; Robb, M. A.; Cheeseman, J. R.; Scalmani, G.; Barone, V.; Mennucci, B.; Petersson, G. A.; Nakatsuji, H.; Caricato, M.; Li, X.; Hratchian, H. P.; Izmaylov, A. F.; Bloino, J.; Zheng, G.; Sonnenberg, L.; Hada, M.; Ehara, M.; Toyota, K.; Fukuda, R.; Hasegawa, J.; Ishida, M.; Nakajima, T.; Honda, Y.; Kitao, O.; Nakai, H.; Vreven, T.; Montgomery, J. A.; Peralta, J. E.; Ogliaro, F.; Bearpark, M.; Heyd, J. J.; Brothers, E.; Kudin, K. N.; Staroverov, V. N.; Kobayashi, R.; Normand, J.; Raghavachari, K.; Rendell, A.; Burant, J. C.; Iyengar, S. S.; Tomasi, J.; Cossi, M.; Rega, N.; Millam, J. M.; Klene, M.; Knox, J. E.; Cross, J. B.; Bakken, V.; Adamo, C.; Jaramillo, J.; Gomperts, R.; Stratmann, R. E.; Yazyev, O.; Austin, A. J.; Cammi, R.; Pomelli, C.; Ochterski, J. W.; Martin, R. L.; Morokuma, K.; Zakrzewski, V. G.; Voth, G. A.; Salvador, P.; Dannenberg, J. J.; Dapprich, S.; Daniels, A. D.; Farkas, O.; Foresman, J. B.; Ortiz, J. V.; Cioslowski, J.; Fox, D. J. Gaussian 09 Revision D.01; Gaussian Inc.: Wallingford CT, **2009**.
(68) Becke, A. D. Density-Functional Thermochemistry. III. The Role of Exact Exchange. *J. Chem. Phys.* **1993**, *98* (7), 5648-5652.
(69) Roy, L. E.; Hay, P. J.; Martin, R. L. Revised Basis Sets for the LANL Effective Core Potentials. *J. Chem. Theory Comput.* **2008**, *4* (7), 1029-1031.
(70) Hehre, W. J.; Ditchfield, R.; Pople, J. A. Self-Consistent Molecular Orbital Methods. XII. Further Extensisons of Gaussian-Type Basis Sets for Use in Molecular Orbital Studies of Organic Molecules. *J. Chem. Phys.* **1972**, *56* (5), 2257-2261.
(71) Guerra, C. F.; Snijders, J. G.; te Velde, G.; Baerends, E. J. Towards an Order-N DFT Method. *Theor. Chem. Acc.* **1998**, *99* (6), 391-403.
(72) te Velde, G.; Bickelhaupt, F. M.; Baerends, E. J.; Guerra, C. F.; Van Gisbergen, S. J. A.; Snijders, J. G.; Ziegler, T. Chemistry with ADF. *J. Comput. Chem.* **2001**, *22* (9), 931-967.
(73) Schreckenbach, G.; Ziegler, T. Calculation of NMR Shielding Tensors Using Gauge-Including Atomic Orbitals and Modern Denstiy Funcitonal Theory. *J. Phys. Chem.* **1995**, *99* (2), 606-611.
(74) Ernzerhof, M.; Scuseria, G. E. Assessment of the Perdew-Burke-Ernzerhof Exchange-Correlation Functional. *J. Chem. Phys.* **1999**, *110* (11), 5029-5036.
(75) Grimme, S. Accurate Description of van der Waals Complexes by Density Functional Theory Including Empirical Corrections. *J. Comput. Chem.* **2004**, *25* (12), 1463-1473.
(76) van Lenthe, E.; Baerends, E. J. Optimized Slater-Type Basis Sets for the Elements 1-118. *J. Comput. Chem.* **2003**, *24* (9), 1142-1156.
(77) van Lenthe, E.; Ehlers, A.; Baerends, E. J. Geometry Optimizations in the Zero Order Regular Approximation for Relativistic Effects. *J. Chem. Phys.* **1999**, *110* (18), 8943-8953.
(78) van Lenthe, E.; Baerends, E. J.; Snijders, J. G. Relativistic Regular 2-Component Hamiltonians. *J. Chem. Phys.* **1993**, *99* (6), 4597-4610.
(79) van Lenthe, E.; Baerends, E. J.; Snijders, J. G. Relativistic Total-Energy Using Regular Approximations. *J. Chem. Phys.* **1994**, *101* (11), 9783-9792.

SYNOPSIS TOC

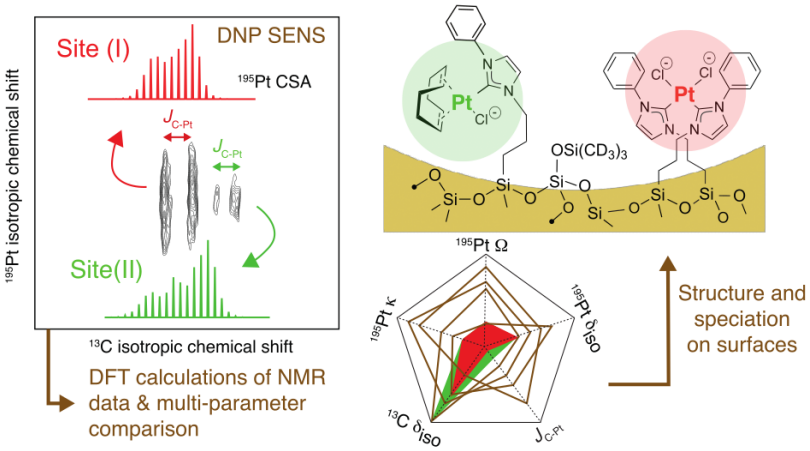

DNP Surface Enhanced NMR spectroscopy in combination with multi-parameter DFT calculations reveal the speciation and structure of Pt-NHC surface complexes.